



Microseismicity Characteristics Before and After a Rockburst and Mechanisms of Intermittent Rockbursts in a Water Diversion Tunnel

Yucheng Wang¹ · Chun'an Tang^{1,2} · Liexian Tang³ · Shichao Zhang¹ · Limin Li⁴ · Yubo Li⁴ · Wenshuo Duan²

Received: 28 November 2020 / Accepted: 28 September 2021 / Published online: 16 October 2021
© The Author(s), under exclusive licence to Springer-Verlag GmbH Austria, part of Springer Nature 2021

Abstract

As the buried depth of the tunnel increased, rockbursts occurred frequently during the tunnel boring machine (TBM) excavation of a diversion tunnel. In addition, multiple rockbursts occurred in the same area within a short period of time, seriously threatening the safety of workers and construction equipment. To understand the evolutionary process of intermittent rockbursts (more than one rockburst occurring in the same area), a real-time microseismic (MS) monitoring system was established. Two typical intermittent rockbursts were investigated to study the microseismicity characteristics before and after each rockburst. By further analyzing the MS event count, cumulative MS energy, energy index, cumulative apparent volume, and E_s/E_p values before and after each rockburst, some seismic precursors to the two intermittent rockbursts were identified. Finally, we elucidated the mechanisms of the two intermittent rockbursts by analyzing the spatial transfer characteristics of MS events with different energies. The results of this study will be useful for intermittent rockburst warning and prevention in the construction of deep tunnels.

Keywords Intermittent rockburst · Microseismic monitoring · Precursor · Rockburst mechanism

List of Symbols

E	Seismic energy
ρ	Rock mass density
c	Velocity of the elastic wave
R	Source radius
J_c	Integral of the particle motion velocity
F_c	Experience coefficient of seismic wave radiation type
E_s	S-wave energy
E_p	P-wave energy
σ_A	Apparent stress

M_0	Seismic moment
μ	Shear modulus of the rock mass
V_A	Apparent volume
EI	Energy index
$E(M_0)$	Average seismic energy
c_1, c_2	Fitting constants

1 Introduction

A rockburst is a dynamic disaster in which the strain energy stored in the rock mass is released instantly during underground engineering excavation, accompanied by sound and the ejection of rock fragments. Moreover, the occurrence of rockbursts is random, sudden, and violent, which greatly increases the difficulty of construction (Ortlepp and Stacey 1994; Hoek et al. 2000). To better regulate rockbursts, several scholars have comprehensively researched the evolution characteristics and control strategies of rockbursts in deep underground engineering. However, rockbursts, which are affected by factors such as ground stress, geological conditions, and excavation methods, exhibit different types. For underground tunnel engineering, there are two recognized rockburst classification methods. (1) Based on the geological

✉ Chun'an Tang
tca@mail.neu.edu.cn

¹ School of Resources and Civil Engineering, Northeastern University, Shenyang 110819, Liaoning, China
² State Key Laboratory of Coastal and Offshore Engineering, School of Civil Engineering, Dalian University of Technology, Dalian 116024, Liaoning, China
³ School of Mining Engineering, University of Science and Technology Liaoning, Anshan 114051, Liaoning, China
⁴ China Railway First Survey and Design Institute Group Ltd., Xi'an 710043, Shanxi, China

conditions and tectonic stress characteristics, rockbursts can be divided into strain-type rockbursts and fault slip-type rockbursts (Gill et al. 1993). (2) Based on the spatiotemporal characteristics, rockbursts can be divided into imminent rockbursts and delayed rockbursts (Chen et al. 2012; Feng et al. 2012b). However, with increased research and an improved understanding of rockbursts, many different types of rockbursts have been discovered and defined. Tang et al. (2010) suggested that for rockburst monitoring and prediction in tunnels, a special attention should be paid to the effects of structural planes. Through detailed investigation and analysis of four extremely intense rockburst cases in a deep tunnel, Zhang et al. (2012) concluded that structural planes play an important role in the occurrence of rockbursts. Based on the previous studies, Feng et al. (2012a) added a class of strain–structure slip rockbursts. Zhou et al. (2015) analyzed the occurrence mechanism of structure-type rockbursts in the deep tunnels of the Jinping-II Hydropower Station, and divided the structure-type rockbursts into a slip type, shear-fracture type, and tension extensile spalling type. Feng et al. (2019b) referred to the occurrence of multiple rockbursts in a particular area as an intermittent rockburst.

With an increasing buried depth of the tunnel, some intermittent rockbursts also occurred in the northern Qinling tunnel boring machine (TBM) construction section of the Hanjiang-to-Weihe River Diversion Project. Moreover, the interval between two rockbursts was generally less than 2 days, which seriously threatened the safety of equipment and workers. Therefore, it is very important to study the evolution process and formation mechanism of intermittent rockbursts.

Microseismic (MS) monitoring, which is a three-dimensional monitoring technology for rock mass, can accurately capture the elastic wave released when microcracks occur in rock masses. This technology can obtain information on the time, location, and intensity of microcrack events through waveform analysis, and can be used to provide an early warning for rock instability (Cai et al. 2001; Tang et al. 2010; Ma et al. 2018). Ma et al. (2015) used MS monitoring to provide early warnings of rockbursts at the Jinping II Hydropower Station and summarized the MS precursor information of the rockbursts. Liu et al. (2018b) analyzed the evolution process of three intense rockbursts along a structural plane using MS monitoring and obtained some unique precursors of structure-type rockbursts. Liu et al. (2020) studied the relationship between small-scale structural planes and rockbursts by analyzing the MS characteristics during the development of structure-type rockbursts and proposed prevention measures based on MS monitoring. By analyzing abundant MS monitoring data, Xue et al. (2020) obtained the precursor characteristics and formation mechanism of rockbursts and proposed a rockburst risk assessment method based on lgN/b . Li et al. (2019) analyzed the MS characteristics across

the lithologic interface from different directions. Feng et al. (2019a) analyzed the influence of structural planes on the MS evolution during rockbursts. Zhang et al. (2020) revealed the MS characteristics of delayed rockbursts and obtained precursor information. By analyzing the MS characteristics of three rockbursts occurring at different positions with respect to a tunnel cross-section, Hu et al. (2019) clarified the influence of the structural plane on the distribution of rockbursts. Ma et al. (2020) established a new method (the EMS method) to reveal the different precursor characteristics of rockburst and fall of ground. Feng et al. (2019b) proposed a definition for intermittent rockbursts and obtained some precursors of intermittent rockbursts based on MS monitoring. It is clear from these previous studies that the evolution of rockbursts can be obtained through MS monitoring, but further research needs to be conducted on the interpretation and warning of intermittent rockbursts.

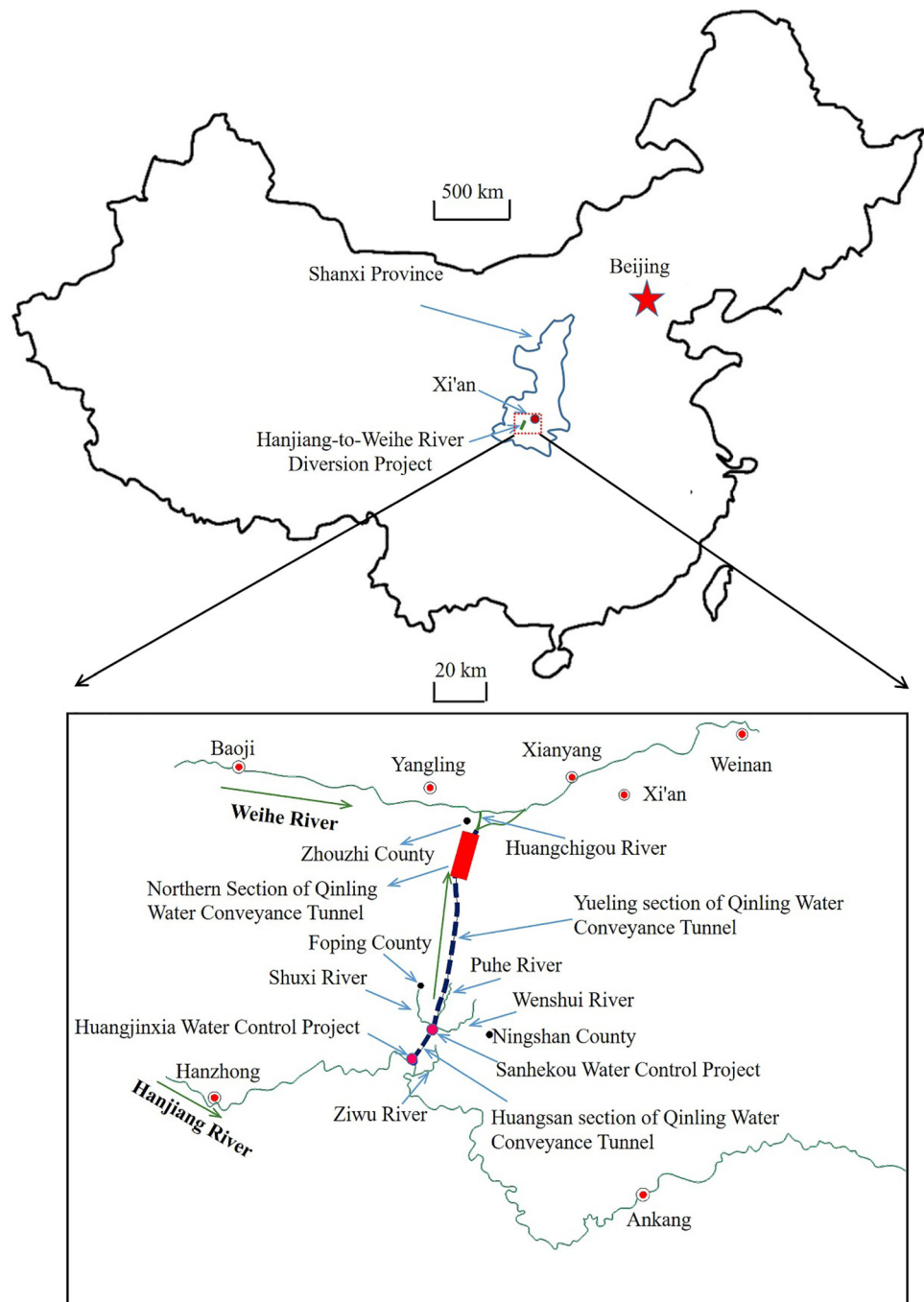
In this paper, we first introduce the MS monitoring system installed in the northern Qinling TBM construction section of the Hanjiang-to-Weihe River Diversion Project. Then, two typical intermittent rockbursts are summarized in detail. Finally, the precursors and formation mechanisms of two typical intermittent rockbursts are analyzed based on the recorded MS monitoring data.

2 Project Overview

2.1 Overview of the Hanjiang-to-Weihe River Diversion Project

The Hanjiang-to-Weihe River Diversion Project, located in Shaanxi Province of northwest China, transports the water from the Han River to the Weihe River to alleviate the problem of water shortage in the cities and industries along the Weihe River. The project consists of three parts: the Huangjinxia Water Control Project, the Sanhekou Water Control Project, and the Qinling Water Conveyance Tunnel, as shown in Fig. 1. The Qinling water conveyance tunnel consists of the Yueling section tunnel with an axis length of 81.77 km and the Huangshan section tunnel with an axis length of 16.52 km. The Huangshan section tunnel, which has a slope of 1/2500, is to transport the Hanjiang water from the Huangjinxia Water Control project to the Sanhekou Water Control Project. The Yueling section tunnel with the maximum depth of 2012 m and a slope of 1/2500, connects the Sanhekou Water Control Project with the Huangchigou River. A total of 39.08 km of the tunnel (circular cross-section, 6.92 m/7.52 m in diameter) were excavated using two TBMs. The remaining 42.69 km of the tunnel (horseshoe cross-section, 6.76 m in diameter) was constructed by the drilling and blasting method.

Fig. 1 Location of the Hanjiang-to-Weihe River Diversion Project



The length of the northern section of the Qinling tunnel, excavated using TBM, is 16.54 km with mileages ranging from K62+902 to K46+360 m. On December 26, 2018, the tunnel was excavated to the mileage of K46+360 m. To speed up the construction of the Qinling tunnel, the northern TBM section was extended 2977 m southward, as illustrated in Fig. 2. The northern TBM excavation section is located in the middle and high mountainous areas of the Qinling Ridge with overburden depths ranging from 553 to 1880 m. The northern TBM excavation section traverses the

Li County–Zhashui County Variscides and the north Qinling Caledonian fold belt, which belongs to the Qinling fold system. 15 faults cross the northern section of the Qinling tunnel with parameters, as shown in Table 1.

To obtain the in-situ stress, a stress measurement campaign was carried out using the hydraulic fracturing method at the mileage of K46+190 m. The result of the in-situ stress measurement is shown in Table 2. The surrounding rock masses of the northern Qinling TBM construction section mainly consisted of metamorphic sandstone with a uniaxial

Fig. 2 Layout of the northern section of the Qinling tunnel of the Hanjiang-to-Weihe River Diversion Project

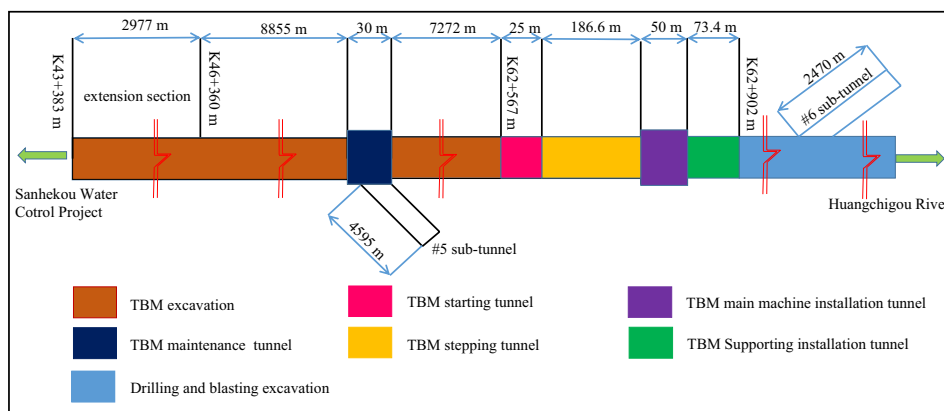


Table 1 Fault parameters of the northern section of the Qinling tunnel

Fault name	Orientation	Fault type	Infilling
f_8	N85°W/65°–75°S	Reverse fault	Cataclasite
f_9	N70°–85°W/65°–75°S	Reverse fault	Cataclasite, Mylonite
f_{10}	N60°–70°E/60°–70°S	Reverse fault	Cataclasite
f_{11}	N75°–85°E/70°–80°S	Reverse fault	Cataclasite
f_{12}	N80°–85°E/70°–80°S	Reverse fault	Cataclasite
f_{13}	N80°–85°W/50°–70°S	Reverse fault	Cataclasite
f_{14}	N75°–80°W/60°S	Reverse fault	Cataclasite
f_{15}	EW–N70°W/50°–75°S	Reverse fault	Cataclasite, Mylonite
f_{16}	N85°E–EW/60°–70°S	Reverse fault	Cataclasite
f_{17}	N85°E–EW/60°–70°S	Reverse fault	Mylonite, Cataclasite
QF ₃	N80°E/60°–70°N	Reverse fault	Cataclasite, Fault Gravel
QF ₃₋₁	N75°–85°E/60°–80°N	Reverse fault	Cataclasite, Fault Breccia
QF ₃₋₂	N75°–85°E/60°–80°N	Reverse fault	Mylonite, Cataclasite
QF ₃₋₃	N75°–85°E/60°–80°N	Reverse fault	Fault Gravel, Cataclasite
QF ₄	N60–80 W/70–80S	Reverse fault	Mylonite

Table 2 Result of the in-situ stress measurement

In situ stress	Value (MPa)	Azimuth angle (°)	Dip angle (°)
σ_1	65.01	269	9
σ_2	49.56	11	48
σ_3	26.82	172	40

compressive strength of 80.2–108.4 MPa and diorite with a uniaxial compressive strength of 127.3–167.7 MPa. Figure 3 shows the geological profile of the Qinling tunnel from mileages K47 + 500 to K43 + 383 m.

2.2 Description of the Intermittent Rockbursts

With an increasing buried depth of the tunnel and corresponding change in the lithology of the rock mass, the frequency and intensity of rockbursts in the northern Qinling TBM construction section increased significantly.

The intensities of the rockbursts occurred in the tunnel construction are classified using the scales, as shown in Table 3. In addition, multiple rockbursts occurred in the same area or adjacent areas within a short period (with an interval between two rockbursts of generally less than 2 days), referred to as an intermittent rockburst (Feng et al. 2019b). Two typical intermittent rockburst cases are shown in Fig. 4.

Case 1 (Fig. 4a) occurred at 08:28 on January 6, 2020. When the working face of the tunnel reached mileage K45 + 703 m, a moderate rockburst occurred in the right sidewall from mileages K45 + 716 to K45 + 710 m. The rockburst pit was 6 m in length, 4 m in width, and 0.9 m deep. During this rockburst, a volume of rock mass fragments was ejected from the rockburst area accompanied by cracking sounds similar to a detonator blasting inside the rock mass. However, approximately 35 h later at 19:47 on January 7, 2020, when the working face of the tunnel reached mileage K45 + 701 m, an intense rockburst occurred in the first rockburst area accompanied by

Fig. 3 Geological profile of the Qinling tunnel from mileages K47 + 500 to K43 + 383 m

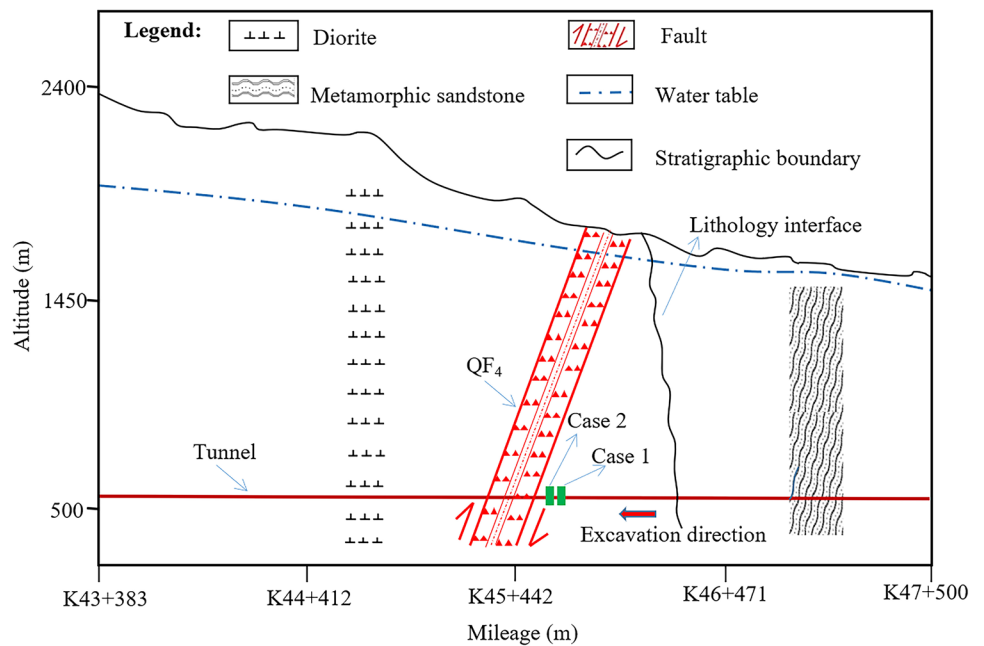


Table 3 Rockburst intensity classification for the Hanjiang-to-Weihe River Diversion Project

Rockburst levels	Main characteristics of rockburst
Mild	There are slight cracking and peeling of rock on the surface of the tunnel without ejection of rock blocks. Cracking and tearing sounds can be heard occasionally. The depths of rockburst craters are generally less than 0.5 m
Moderate	There are obvious cracking and peeling on the surface of the tunnel with slight ejection of rock blocks. Cracking and tearing sounds like a detonator blasting inside the rock mass can be heard. The depths of rockburst craters range from 0.5 to 1.5 m
Intense	There are severe crackings in the surface of the tunnel with intense ejection of rock blocks and rock powder. Failure sounds can be heard like a blasting burst sound inside the rock mass and last for a long time. The depths of rockburst craters range from 1.5 to 3.0 m, which has a severe influence on TBM construction
Extremely intense	There are large-scale severe rockbursts and large pieces of rock blocks are ejected violently. Ground vibration is strong, accompanied by loud sounds like a thunder. The depths of rockburst craters are greater than 3.0 m, and the entire tunnel construction section is severely damaged

cracking sounds similar to an explosive blast. The depth of the rockburst pit was 2.2 m.

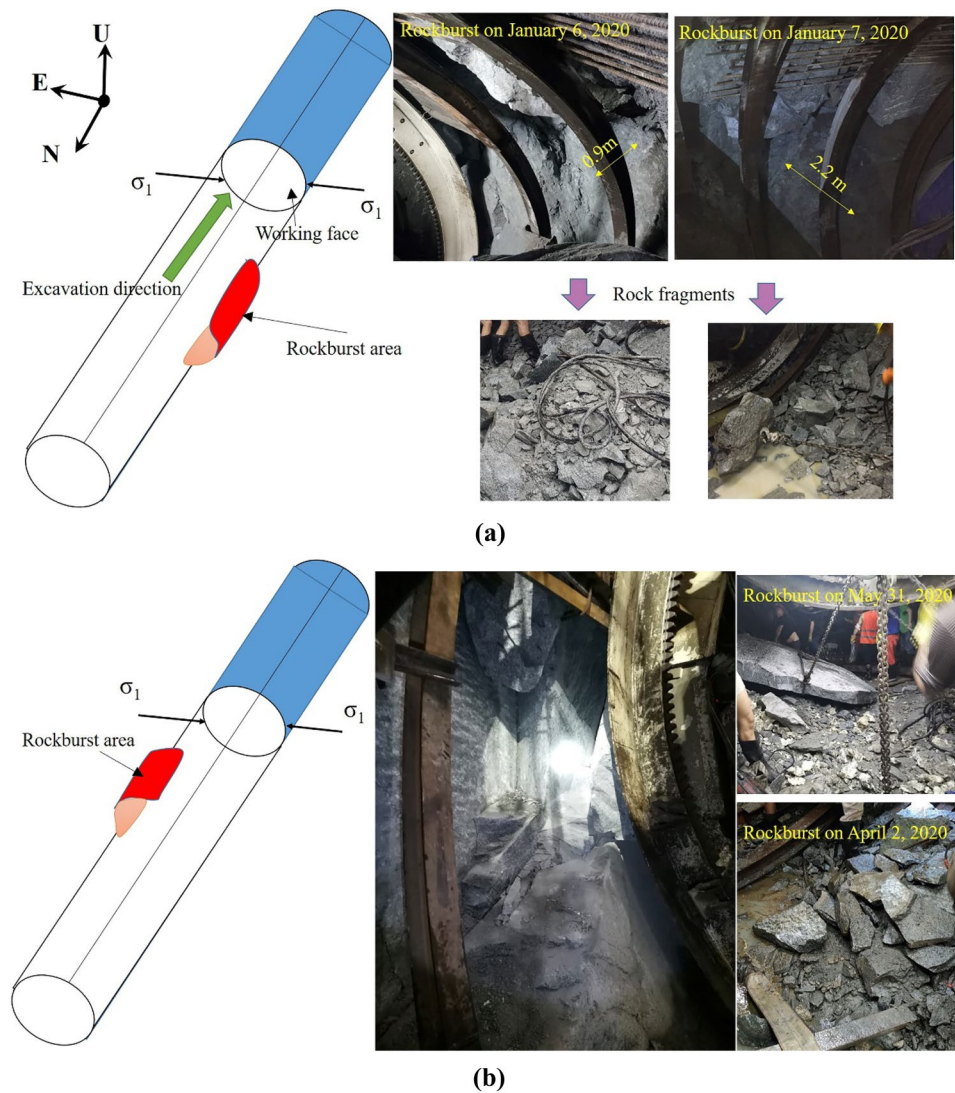
Case 2 (Fig. 4b) occurred at 04:35 on March 31, 2020. When the working face of the tunnel reached mileage K45 + 588 m, an intense rockburst occurred in the left sidewall from mileages K45 + 600 to K45 + 592 m. According to the data recorded by the site engineer, the depth of the rockburst pit was 1.8 m, and the dimensions of the largest rock fragment were 2.4 m in length, 1.6 m in width, and 0.8 m in height. However, approximately 39 h later at 19:35 on April 1, 2020, a moderate rockburst occurred in the area of the first rockburst accompanied by crisp sounds and the ejection of small rock fragments. The depth of the rockburst pit was 0.6 m.

3 In Situ MS Monitoring

3.1 Brief Introduction of MS Monitoring System

The MS monitoring system used for the project is manufactured by Engineering Solution Group (ESG) of Canada. The system consists of a digital signal acquisition system, six uniaxial accelerometers, and a Hyperion digital signal processing system. Due to high strength and good continuity of the rock mass, the elastic wave generated by the rock mass failure tends to have a high frequency and the attenuation is low. Therefore, accelerometers with a sensitivity of 30 V/g and a frequency response range

Fig. 4 Rockburst damage: **a** Case 1 and **b** Case 2



of 50 Hz–5 kHz were selected. The Paladin data acquisition system has an acquisition frequency of 10 kHz and a 24 bit analog-to-digital (A/D) converter. The Paladin data acquisition system was placed in a metal box, which was suspended on the tunnel wall by wires and anchoring agents. The optical cable was suspended from the steel arch, and the power cord was connected to the lighting circuit attached to the tunnel wall. The accelerometer array was placed 70 m behind the tunnel face to ensure personnel and equipment safety. Six accelerometers were installed in the 3.5 m-deep boreholes of the tunnel side-walls with anchoring agents and were distributed at two cross-sections with an interval of 50 m. When the tunnel face moves forward by 50 m, the accelerometers of the last section were recycled and installed in a new front monitoring section to ensure continuous monitoring. The MS monitoring system was completely separated from the TBM tunneling system, and this reduced the influence of

TBM excavation on MS monitoring. The layout of the MS monitoring system is shown in Fig. 5.

3.2 Recognition of MS Signals

In the excavation process of the northern section of the Qinling tunnel, the construction conditions were complex, and the MS monitoring equipment captured numerous noise signals such as TBM vibration signals, bolt-drilling knock signals, natural earthquake signals, and unknown noise signals. A large number of noise signals were mixed with the MS signals, which greatly increased the difficulty of identifying effective MS events and interfered with the subsequent analysis of the laws of MS activities. Therefore, it was necessary to understand the characteristics of various signals. Fast Fourier transform (FFT), a spectrum analysis method, is widely used to convert the digital signal series in the time-domain to a signal series in the frequency domain.

Fig. 5 MS monitoring system configuration for field monitoring at the northern section of the Qinling tunnel

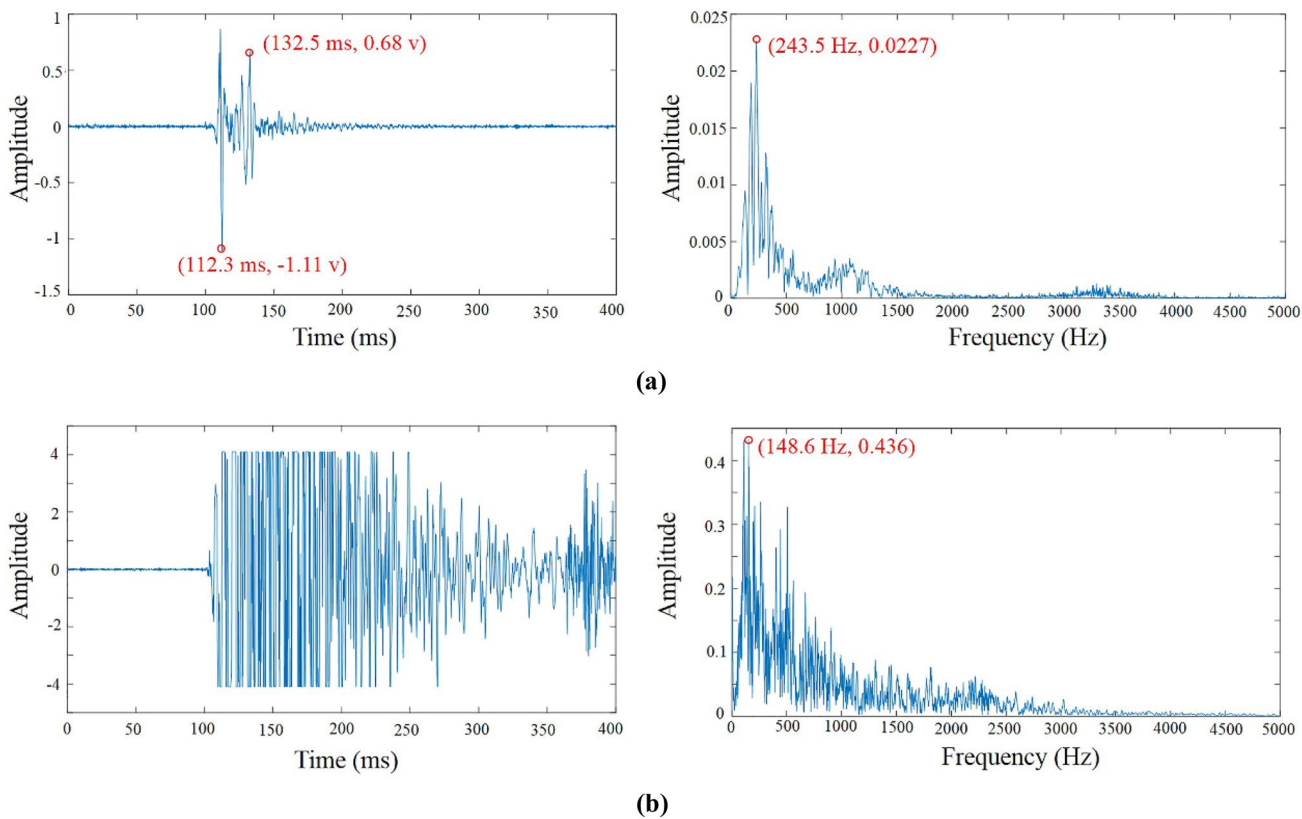
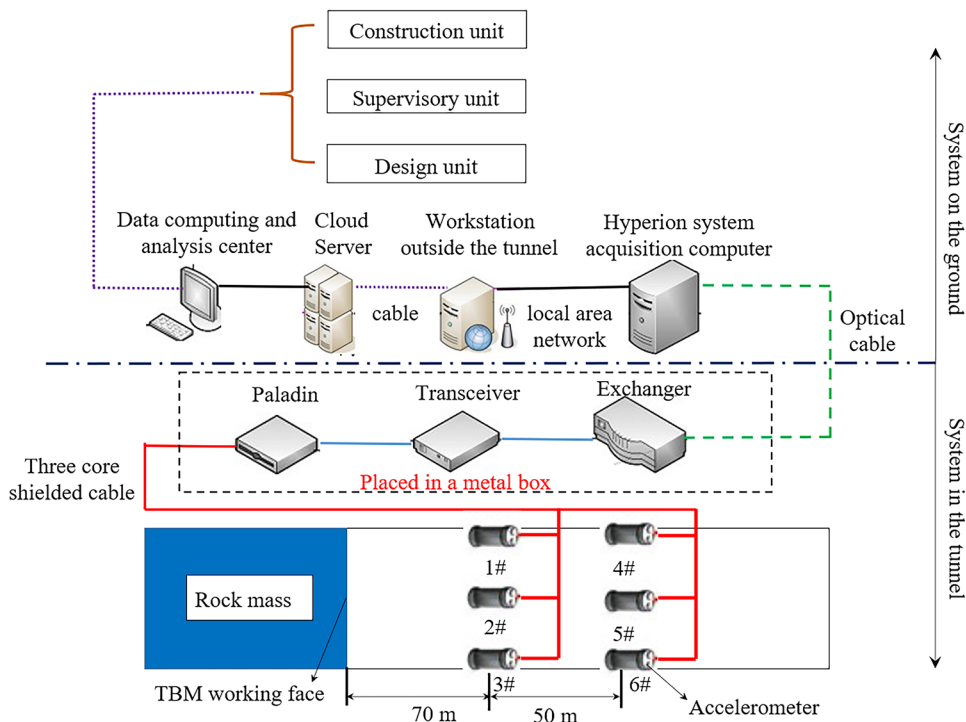


Fig. 6 Waveform analysis of different signals from the northern section of the Qinling tunnel in both the time- and frequency-domains: **a** MS event, **b** rockburst, **c** TBM vibration, **d** bolt-drilling machine, and **e** natural earthquake

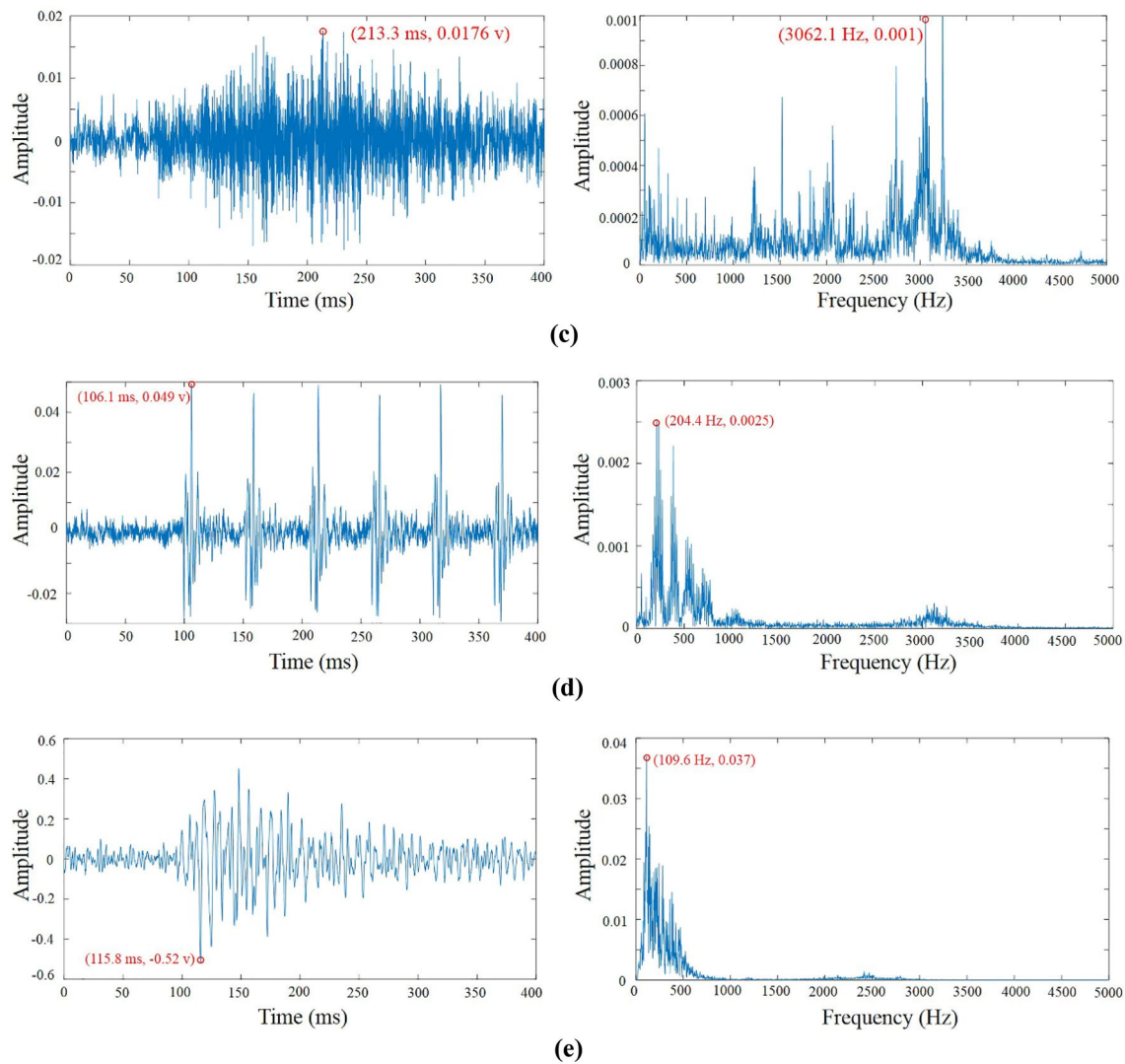


Fig. 6 (continued)

Figure 6 shows the characteristics of common signals in both the time- and frequency-domains.

Figure 6a shows the waveform of an MS event. We can see that the amplitude of the MS event rapidly increased to 1.11 V at 112.3 ms. Subsequently, the amplitude increased rapidly again to 0.68 V at 132.5 ms after a short period of decrease, which may be related to the superposition of the P-wave and S-wave. Therefore, it is easy to identify the arrival times of the P-wave and S-wave based on the above waveform characteristics. Moreover, the dominant frequency distribution was concentrated, distributed within approximately 50–400 Hz, and the main frequency value was 243.5 Hz.

A rockburst signal in both the time- and frequency-domains is shown in Fig. 6b. The amplitude of the rockburst rapidly increased to a maximum of 4.1 V, which lasted approximately 126 ms. Subsequently, the amplitude

of the rockburst gradually attenuated with the developed coda. As a result, it is easy to identify the arrival time of the P-wave, but difficult to identify the arrival time of the S-wave. Moreover, the dominant frequency range of the signal was approximately 20–1000 Hz and the main frequency was 148.6 Hz. Compared with an MS event, the amplitude of a rockburst signal was relatively large and the main frequency value was relatively low.

Figure 6c shows the waveform of a TBM vibration signal. The duration of the TBM vibration signal was relatively long and was not fully acquired owing to the limitation of the sampling time. It is difficult to determine the arrival time of the S-wave. The dominant frequency distribution range was relatively wide, about 1200–3300 Hz, and the distribution of 2600–3300 Hz was the most concentrated; the main frequency value was 3062.1 Hz. Compared with an MS event, the amplitude of a TBM vibration

signal was relatively low and the main frequency value was relatively large.

Figure 6d shows the waveform of a bolt-drilling machine vibration signal. The bolt-drilling machine vibration signal in the amplitude–time curve has multiple peaks, and the maximum amplitude was approximately 0.049 V. Moreover, the dominant frequency range of the signal was approximately 100–700 Hz and the main frequency was 204.4 Hz.

Figure 6e shows the waveform of a natural earthquake that occurred in the Qinling area. It is easy to identify the arrival times of the P-wave and S-wave. The dominant frequency range of the signal was approximately 50–500 Hz and the main frequency was 109.6 Hz.

Note that the natural earthquake signals occurred occasionally, and a large number of bolt-drilling machine vibration signals were concentrated in a certain period of time. Therefore, the above two signals have negligible influence on the MS event signals. Moreover, there were only a small number of MS events during TBM excavation process of the northern section of the Qinling tunnel. Therefore, most MS events were very pure, with high signal-to-noise ratios. For a small amount of MS event signals disturbed by TBM vibration signals, we can filter out the noise signals through the difference between the two signals in frequency. Ten groups of original data with noise mixing were selected for analysis. The signal-to-noise ratios of ten groups of original signals after processing were distributed within the range of 26.5–43.8 dB.

3.3 MS Wave Velocity Measurement

When the source is located outside the accelerometer array, the uncertainty of the wave velocity of the rock mass is the major factor that influences the source location error. The accelerometer array is placed 70 m behind the tunnel face, which means that most MS events occurred outside the accelerometer array. Therefore, the determination and calibration of the wave velocity are important to reduce the source location error. Fixed-point knock experiment was carried out to calibrate the P-wave velocity. Using the position of the knock point as a known point source, the source location error of the known knock point at different wave velocities was analyzed. According to the geophysical test results, the P-wave velocities of the rock mass were in the range of 5000–6000 m/s. We analyzed the source location error of four knock experiments using P-wave velocities from 5000 to 6000 m/s with an interval of 100 m/s, and the results are presented in Fig. 7. When the P-wave velocity was 5700 m/s, the average error of the four knock experiments reached the minimum of 3.44 m. In addition, the wave velocity needed to be corrected in real time to ensure the accuracy of the source location according to the changes of the geological conditions along the tunnel. To facilitate

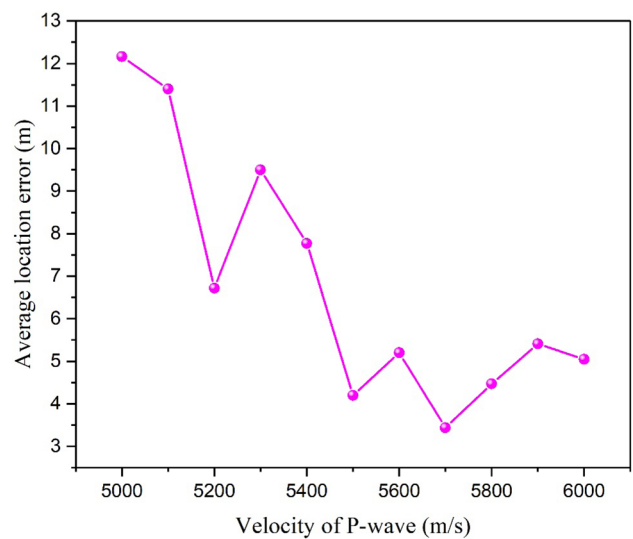


Fig. 7 Source location error of fixed-point knock tests with different P-wave velocities

the operation, we modified the wave velocity based on the comparison between the monitored position of the strong seismic source and the actual position recorded in the field. For example, when the rock type changed from metamorphic sandstone to diorite, we modified the wave velocity from 5700 to 5500 m/s using the method described above.

3.4 Quantification of Source Parameters

MS energy, reflecting intensity of rock mass failure, is an important parameter in MS monitoring. Therefore, (Liu et al. 2018a; Xu et al. 2015) revealed the failure degree of the rock mass by analyzing the evolution law of MS energy. The MS energy, caused by elastic strain energy transforming into inelastic strain energy during rock mass failure, can be determined from the recorded waveforms as (Boatwright and Fletcher 1984)

$$E = 4\pi\rho cR^2 \frac{J_c}{F_c^2}, \tag{1}$$

where E is the energy released by a microcrack, ρ is the rock mass density, c is the velocity of the elastic wave, R is the source radius, J_c is the integral of the particle motion velocity, and F_c is the experience coefficient of seismic wave radiation type. Moreover, the total MS energy can be estimated by S-wave energy (E_s) and the P-wave energy (E_p), as follows:

$$E = E_s + E_p. \tag{2}$$

In seismology, the ratio of S- to P-wave energy E_s/E_p is an important parameter that reflects the seismic source

mechanism of earthquakes (Gibowicz et al. 1991). Since then, many studies on the distribution of MS events with different E_s/E_p values have been undertaken. Three typical results are summarized in Table 4.

The proportion of tensile failure events is very high during the process of a strainburst. Moreover, a strain–structure slip rockburst occurred in the form of shear failure. Therefore, we analyzed the distribution of 646 MS events with different E_s/E_p values during the processes of five strainbursts, and found that MS events with E_s/E_p values less than 3 accounted for 96.4%. This result suggests that the upper bound of E_s/E_p value for tensile failure may be 3. In addition, 20 main seismic events with different E_s/E_p values during the processes of 20 strain–structure slip rockbursts were investigated, and found that E_s/E_p values of 18 main seismic events were distributed between 10 and 30, while the others were greater than 30. This result suggests that the lower bound of E_s/E_p value for shear failure may be 10. Therefore, the criteria for determining the seismic source failure mechanism based on the energy ratio can be summarized as

$$\begin{cases} \text{Tension failure } E_s/E_p < 3 \\ \text{Mixed failure } 3 \ll E_s/E_p \leq 10. \\ \text{Shear failure } 10 < E_s/E_p \end{cases} \quad (3)$$

The apparent volume and apparent stress are often used to describe the variation of rock mass before the earthquake. The apparent stress is defined as the radiated energy of the source inelastic deformation (Wyss and Brune 1968), as follows:

$$\sigma_A = \frac{\mu E}{M_0}, \quad (4)$$

where σ_A is the apparent stress, M_0 is the seismic moment, E is the seismic energy, and μ is the shear modulus of the rock mass. The apparent volume represents the volume of rock mass with the source inelastic deformation, as follows (Mendecki 1993):

$$V_A = \frac{M_0}{2\sigma_A} = \frac{M_0^2}{2\mu E}, \quad (5)$$

where V_A is the apparent volume.

In seismology, there is a positive correlation between energy index and apparent stress. Therefore, the energy

index actually reflects the stress level of the monitoring area. The energy index of an MS event is the ratio of the observed radiated seismic energy of that event to the average energy radiated by events of the same seismic moment, as follows (Van Aswegen and Butler 1993):

$$EI = \frac{E}{\bar{E}(M_0)}, \quad (6)$$

where EI is the energy index and $\bar{E}(M_0)$ is the average seismic energy. Moreover, the average seismic energy can be taken from the relationship between $\log E$ and $\log M_0$ for the area of interest, as follows:

$$\log \bar{E}(M_0) = c_1 \log M_0 + c_2, \quad (7)$$

where c_1 and c_2 are the fitted constants, which can be obtained from the linear fitting of the MS energy and seismic moment. For example, Fig. 8 shows the energies and seismic moments of 146 MS events and the relationship between the energy and seismic moment during two rockbursts of Case 1. Thus, the energy index can be estimated by combining Eqs. (6) and (7)

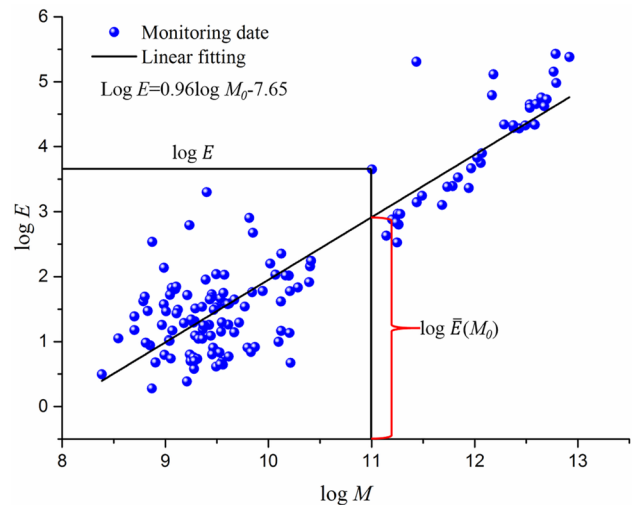


Fig. 8 Relationship between the energies and seismic moments of MS events in Case 1

Table 4 Distribution of MS events with different E_s/E_p values

Serial number	Failure mechanism of rock mass			References
	Tensile failure	Mixed failure	Shear failure	
1	$E_s/E_p < 1$	$1 \leq E_s/E_p \leq 4.5$	$E_s/E_p > 4.5$	(Salvoni and Dight 2016)
2	$E_s/E_p < 10$	$10 \leq E_s/E_p \leq 20$	$E_s/E_p > 20$	(Xiao et al. 2016)
3	$E_s/E_p < 3$	$3 \leq E_s/E_p \leq 10$	$E_s/E_p > 10$	(Liu et al. 2020; Xue et al. 2020)

$$EI = \frac{10^{7.65} E}{M_0^{0.96}} \tag{8}$$

4 Microseismicity Characteristics Before and After Each Rockburst

4.1 Case 1

The temporal evolution of the MS event count and cumulative MS energy in Case 1 are illustrated by the purple bar and black curve in Fig. 9. Similar to previous studies (Liu et al. 2018a, b, 2020), the MS event count experienced a rapid rise from a low level to a high level before the first rockburst, accompanied by a change in the cumulative MS energy curve from gradual growth to rapid growth. According to Liu et al. (2020), after a rockburst, the MS event count usually declines rapidly to a low level, and the cumulative MS energy curve gradually increases. However, the MS event count remained high and the cumulative MS energy continued to rise rapidly after the first rockburst. These abnormal changes may be related to the degree of energy release in the rock mass. From the green curve in Fig. 9, we can see that the daily maximum MS event energy on January 6, 2020 was much lower than that on January 5, 2020. This observation indicates that the first rockburst released a relatively low amount of energy. Therefore, the energy continued to accumulate rapidly in the rock mass of the first rockburst area, resulting in a large number of high-energy events in the surrounding rock mass. During this stage, the surrounding rock mass was still relatively unstable. Correspondingly, an intense rockburst occurred on January 7, 2020. After the

second rockburst, the MS event count rapidly decreased to a low level, and the cumulative MS energy growth rate dropped rapidly, indicating that the stress release in the rock mass greatly reduced the risk of another rockburst.

The pink and blue curves in Fig. 9 show the temporal evolution of the cumulative apparent volume and energy index in Case 1. The cumulative apparent volume could be seen to increase sharply with time before the rockburst, while the logEI increased rapidly from 0.96 to 2.37 over the same time. According to Liu et al. (2018b), the above changes can be considered precursor characteristics of a rockburst. Then, a moderate rockburst occurred on January 6, 2020. After the first rockburst, the logEI increased to a maximum value of 2.44 after a small decrease, indicating that the stress in the rock mass was not completely released and continued to increase to a high level. Moreover, the cumulative apparent volume increased rapidly, which may mean that the inelastic deformation in the rock mass continued to accumulate rapidly. Therefore, the surrounding rock mass was still unstable and at risk of failure, and an intense rockburst occurred on January 7, 2020. After the second rockburst, the logEI dropped dramatically to a low level, and the cumulative apparent volume increased gradually. This indicates that the stress was effectively released, and the accumulation of inelastic deformation was not obvious after the second rockburst. Therefore, the risk of further rockbursts was relatively low.

Figure 10 shows the distribution of MS events with different E_s/E_p values in Case 1. In the early stage of the first rockburst, the E_s/E_p values fluctuated markedly between 0 and 13, and the type of rock mass failure was dominated by mixed and shear failure. During this stage, the surrounding rock mass was relatively stable. However, the E_s/E_p values

Fig. 9 Temporal evolution of source parameters in Case 1

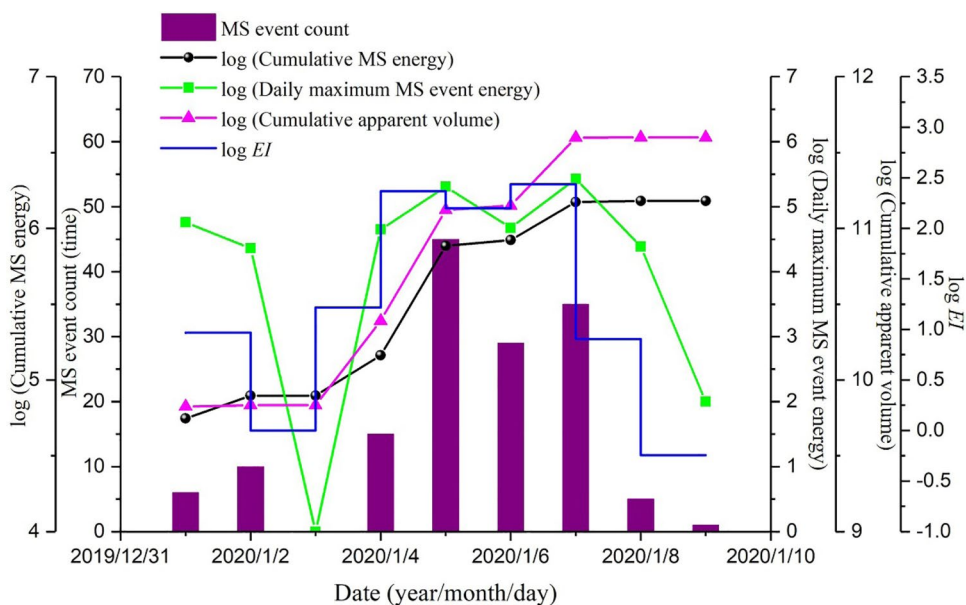
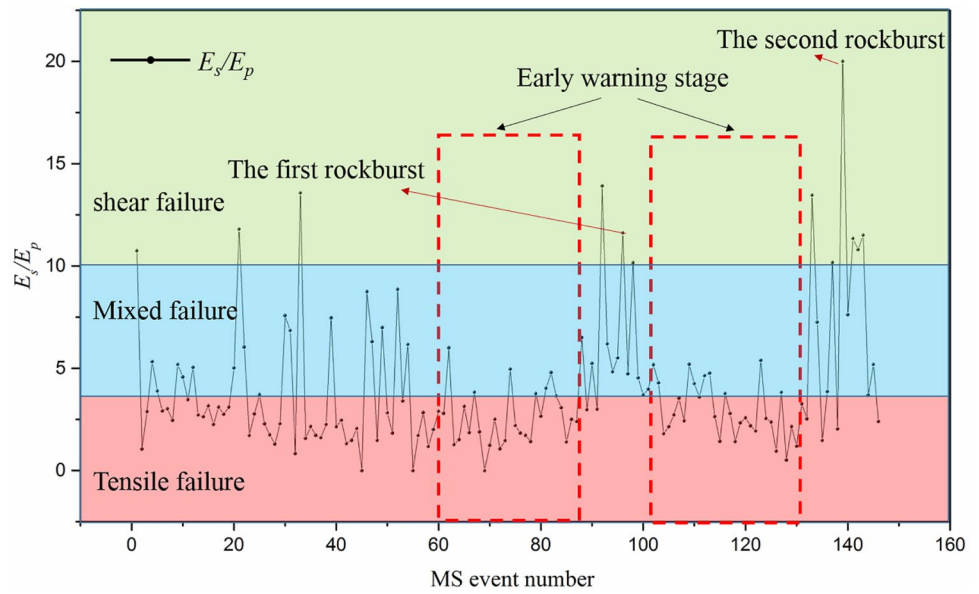


Fig. 10 Distribution of MS events with different E_s/E_p values in Case 1



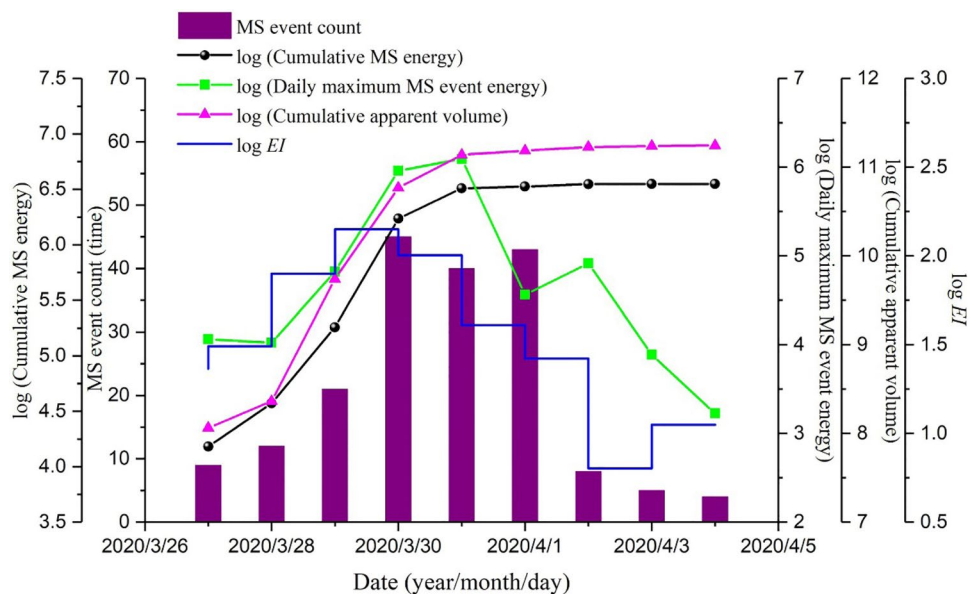
almost dropped to below 3 with time preceding the rockburst, which indicates that the proportion of tensile failure of the surrounding rock mass increased rapidly. During this stage, the surrounding rock mass was unstable and at risk of failure (Xue et al. 2020). Then, a moderate rockburst occurred in the form of shear failure and was accompanied by some shear failure events. After the first rockburst, the E_s/E_p values mostly remained low, and the type of surrounding rock mass failure was mainly tensile failure, which indicates that the surrounding rock mass was still unstable. Subsequently, an intense rockburst occurred in the form of shear failure in the first rockburst area. After the second rockburst, the E_s/E_p values showed a steep upward trend, indicating

that the surrounding rock mass tended to gradually stabilize. Subsequently, no other rockbursts occurred in this rockburst area. From the above analysis, we can see that the E_s/E_p values decreased to low levels before the first and second rockbursts. Therefore, the change in the E_s/E_p values can be used as an indicator for intermittent rockburst warnings.

4.2 Case 2

Similarly, we also analyzed the temporal evolution of the MS event count and cumulative MS energy in Case 2, as shown by the purple bar and black curve in Fig. 11. As mentioned previously, the MS event count and cumulative MS

Fig. 11 Temporal evolution of source parameters in Case 2



energy increased rapidly before the first rockburst in Case 2. However, during the day after the first rockburst, the MS event count remained high, accompanied by an insignificant increase in the cumulative MS energy, which is different from Case 1. From the green curve in Fig. 11, we can see that the first rockburst released a relatively large amount of energy. The remaining energy could not continue to accumulate to a high level, which may be related to the fact that the surrounding rock mass was not capable of storing a large amount energy after the first rockburst, as illustrated in Sect. 5. Therefore, many relatively low-energy MS events were recorded in the surrounding rock mass, and a moderate rockburst occurred on April 2, 2020. After the second rockburst, the MS event count decreased rapidly, and the cumulative MS energy increased gradually. The risk of further rockbursts was relatively low.

The pink and blue curves in Fig. 11 show the evolution of the cumulative apparent volume and energy index in Case 2. The same precursor as in Case 1 was also found. That is, the $\log EI$ increased rapidly from 1.37 to 2.15 accompanied by a rapid increase in the cumulative apparent volume before the first rockburst in Case 2. After the first rockburst, the stress in the surrounding rock mass was released, causing the $\log EI$ to decrease rapidly to 1.6 on April 1, 2020. Meanwhile, the cumulative apparent volume increased gradually. According to Liu et al. (2018b) and Case 1, these variations in the cumulative apparent volume and $\log EI$ indicate that the rockburst risk was relatively low. However, a moderate rockburst occurred at 19:35 on April 1, 2020. After the second rockburst, the $\log EI$ decreased rapidly to a relatively low level of 0.81 accompanied by a gradual increase in the cumulative apparent volume. Subsequently, no other rockbursts occurred in this rockburst area.

Figure 12 shows the distribution of MS events with different E_s/E_p values in Case 2. Similar to Case 1, the E_s/E_p values decreased rapidly to relatively low levels before the two rockbursts of Case 2. In addition, the E_s/E_p values showed an upward trend after the rockburst, indicating that the risk of further rockbursts was low.

4.3 Comparison Between Case 1 and Case 2

Based on the above analysis, the MS characteristics of the different stages of two typical intermittent rockbursts are summarized in Table 5.

Notably, after the first rockburst, there were some similar MS characteristics in Cases 1 and 2, e.g., the MS event count remained high and the E_s/E_p values remained low after a short period of fluctuation. This phenomenon provides a basic reference for evaluating whether another rockburst is likely to occur after an initial rockburst. In practice, we can first preliminarily predict whether another rockburst is likely to occur after a rockburst in a certain area using the evolution characteristics of the MS event count and the E_s/E_p values. Then, we can evaluate the most likely type of intermittent rockburst according to the evolutionary characteristics of the cumulative MS energy, EI , and cumulative apparent volume. Finally, based on the different types of intermittent rockbursts, different measures can be implemented to prevent further rockbursts.

Fig. 12 Distribution of MS events with different E_s/E_p values in Case 2

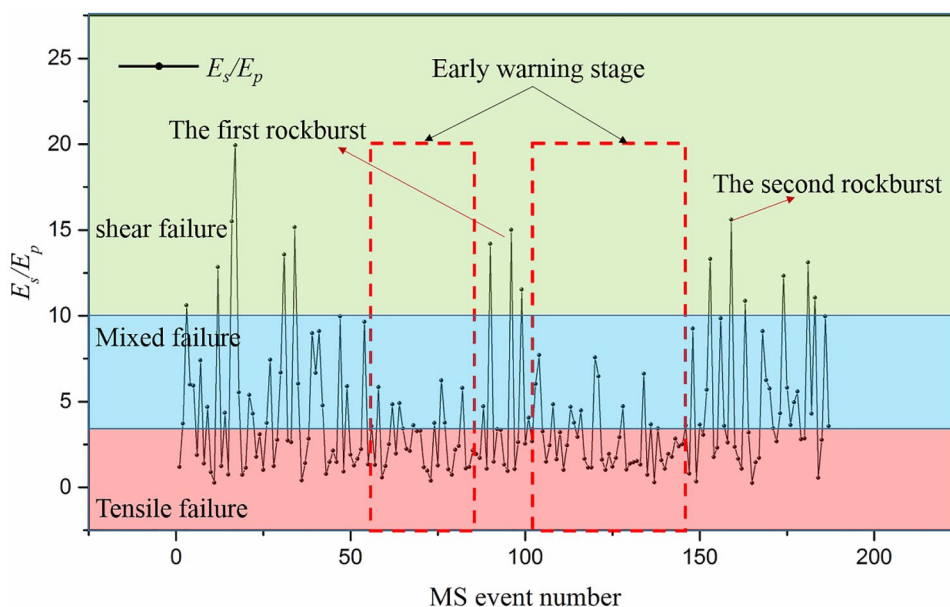


Table 5 Comparison of the microseismicity characteristics of two intermittent rockbursts

Stage	Source parameter	Case 1	Case 2
Before the first rockburst	MS event count and cumulative MS energy	MS event count and cumulative MS energy increased rapidly	MS event count and cumulative MS energy increased rapidly
	Cumulative apparent volume and EI	EI increased rapidly accompanied by a rapid increase in the cumulative apparent volume	EI increased rapidly accompanied by a rapid increase in the cumulative apparent volume
	E_s/E_p	E_s/E_p values decreased to relatively low levels	E_s/E_p values decreased to relatively low levels
After the first rockburst	MS event count and cumulative MS energy	MS event count maintained high and the cumulative MS energy continued to increase rapidly	MS event count maintained high and the cumulative MS energy increased gently
	Cumulative apparent volume and EI	High-level EI continued to increase and the cumulative apparent volume continued to increase rapidly	EI decreased rapidly and the cumulative apparent volume increased gently
	E_s/E_p	E_s/E_p values mostly remained low	E_s/E_p values mostly remained low
After the second rockburst	MS event count and cumulative MS energy	MS event count decreased rapidly and cumulative MS energy increased gently	MS event count decreased rapidly and cumulative MS energy increased gently
	Cumulative apparent volume and EI	EI decreased rapidly and the cumulative apparent volume increased gently	EI decreased rapidly and the cumulative apparent volume increased gently
	E_s/E_p	E_s/E_p values showed an upward trend	E_s/E_p values showed an upward trend

5 Formation Mechanism of Intermittent Rockbursts

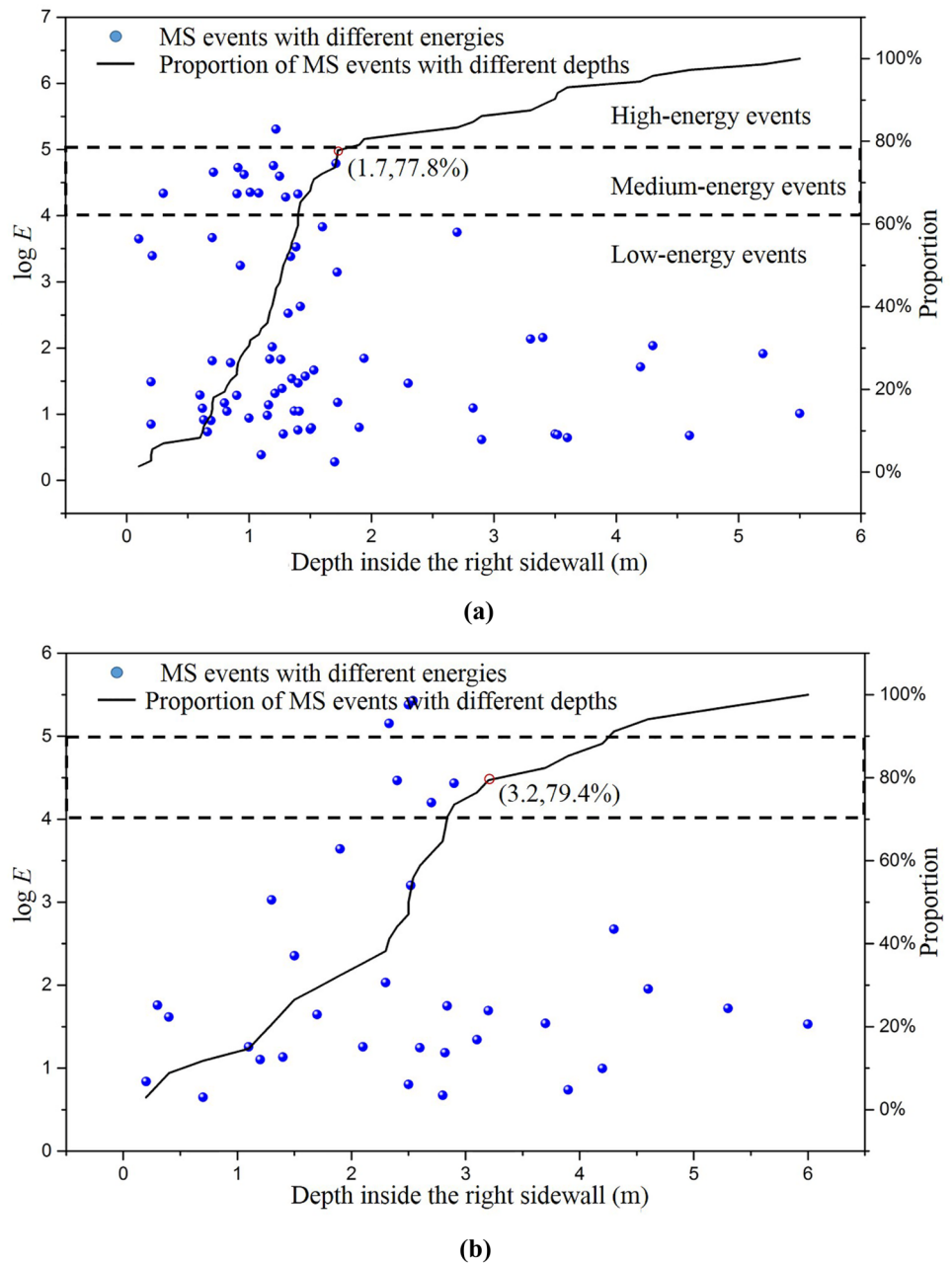
Tunnel excavation induces stress adjustment in surrounding rock mass; the highly concentrated stress leads to fracturing of the rock mass. Therefore, the fracturing of rock mass may be regarded as an external manifestation of stress. Moreover, microcracks occur inside the rock mass, accompanied by the release of stored elastic energy in the form of a stress wave, which can be recognized as MS events by the MS monitoring system. Therefore, microseismicity may indirectly reflect the stress change in rock mass. Based on the 3S theory (stress buildup, stress shadow, and stress transfer), Ma et al. (2015) divided the MS evolution of a rockburst into three phases: the development period, peak period, and quiet period. Before a rockburst, there is usually a peak period of microseismicity due to stress buildup. After a rockburst, there is a quiet period of microseismicity due to the stress shadow. In addition, if there is no MS quiet period after a rockburst, which indicates that the stress in the region has not been completely released and the rockburst risk has not been relieved. Based on the above theory, the mechanism of intermittent rockbursts can be illustrated.

Figure 13 presents the distribution of MS events with different energies inside the right sidewall in Case 1. Before the first rockburst, a total of 72 MS events were captured within 0–5.5 m inside the right sidewall, and 77.8% of those MS events, including all of the medium-energy events (with logarithmic energies of greater than 4 but less than 5) and

high-energy events (with logarithmic energies greater than or equal to 5), occurred within 0–1.7 m inside the right sidewall, as shown in Fig. 13a. This indicates that the high stress was mainly concentrated within 0–1.7 m inside the right sidewall, and the rock mass in this range was unstable. Subsequently, a moderate rockburst occurred on the right sidewall after the working face, forming a rockburst pit with a depth of 0.9 m. After the first rockburst, 34 MS events continued to occur within 0–6.0 m inside the right sidewall, and the proportion of MS events within 0–3.2 m inside the right sidewall accounted for 79.4% of these, as shown in Fig. 13b. It is worth noting that 53.1% of those MS events, including all of the high-energy events, were recorded within 1.5–3.2 m inside the right sidewall, indicating that the high stress in the rockburst area was not sufficiently released, and had transferred to the rock mass within 1.5–3.2 m inside the right sidewall. The rock mass in this range was relatively complete and had the capacity to accumulate high stress. Therefore, large-scale cracks were generated under the high stress. Subsequently, an intense rockburst occurred, forming a rockburst pit with a depth of 2.2 m. After the second rockburst, only a small number of low-energy events (with logarithmic energies of less than 4) were distributed discretely in the surrounding rock mass within the rockburst area, indicating that the stress in the rockburst area was sufficiently released and the stress adjustment had finished.

Figure 14 shows the distribution of MS events with different energies inside the left sidewall in Case 2. Before the first rockburst, 54 MS events were recorded within

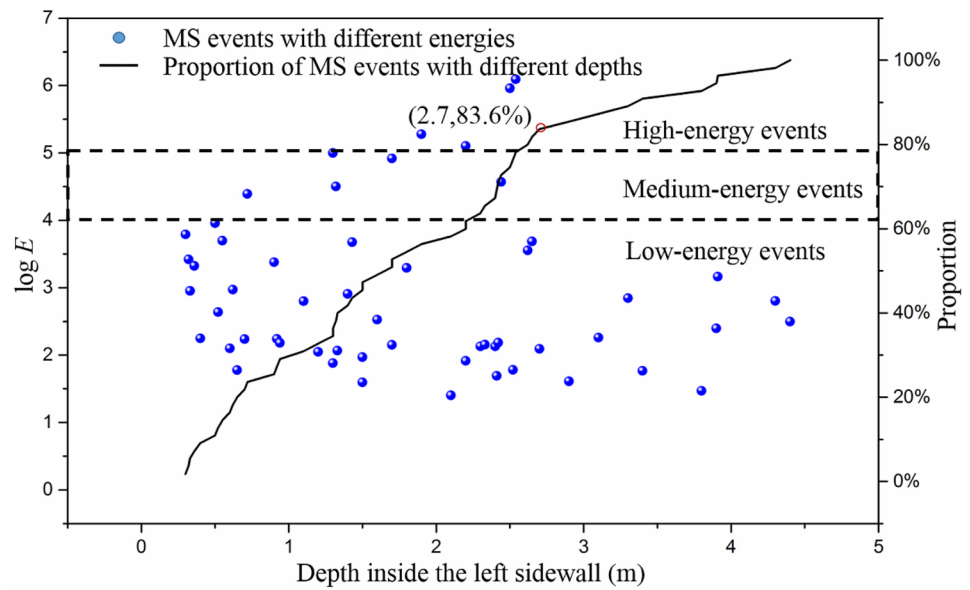
Fig. 13 Distribution of MS events with different energies inside the right sidewall in Case 1: **a** before the first rockburst and **b** between the first and second rockbursts



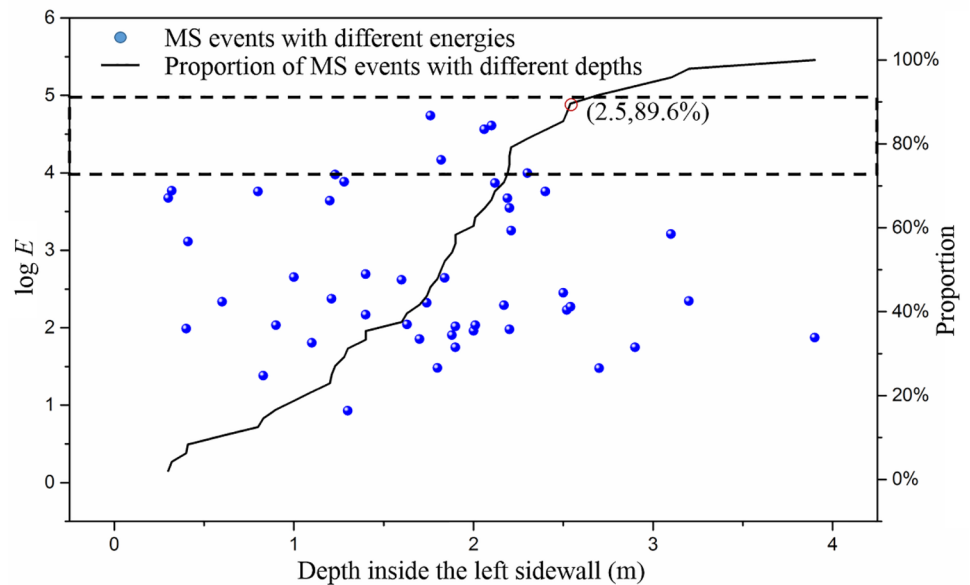
0–4.4 m inside the left sidewall, and 83.4% of those MS events, including four medium-energy events and five high-energy events, were concentrated within 0–2.7 m inside the left sidewall. Moreover, the remaining MS events were distributed within 2.7–4.4 m inside the left sidewall. The distribution of the MS events shows that high stress was mainly concentrated within 0–2.7 m inside the left sidewall, and large-scale cracks were generated within 0–2.7 m inside the left sidewall. Coincidentally, an intense rockburst occurred inside the left sidewall, forming a rockburst pit with a depth of 1.8 m. After the first rockburst, 44 low-energy MS events and 4 medium-energy MS events occurred within 0–3.9 m inside the left sidewall, and 89.6% of those

MS events occurred within 0–2.5 m inside the left sidewall. This result indicates that the stress in the rockburst area was not sufficiently released and continued to accumulate in the rock mass within 0–2.5 m inside the left sidewall. However, affected by the first rockburst, the stress-storage capacity of the rock mass in this range was relatively limited. Therefore, no high-energy MS events continued to occur in this area. Subsequently, a moderate rockburst occurred in the first rockburst area, forming a rockburst pit with a depth of 0.6 m. After the second rockburst, only a few MS events were recorded in the rockburst area in the next 2 days, which indicates that the stress in the rockburst area was sufficiently released and there was low risk of another rockburst.

Fig. 14 Distribution of MS events with different energies inside the left sidewall in Case 2: **a** before the first rockburst and **b** between the first and second rockbursts



(a)



(b)

The above analysis further suggests that some high-energy MS events in relatively deep rock masses of the rockburst area after a rockburst can be used as a characteristic to judge whether another rockburst of the same or higher intensity level may occur. In contrast, the accumulation of a large number of relatively low-energy MS events in the shallow rock mass of the rockburst area after a rockburst can be used as a characteristic to determine whether another lower intensity rockburst may occur. Moreover, it is worth noting that if a small number of low-energy MS events are discretely distributed in the rockburst area after

a rockburst, this can be used as an indicator that further rockbursts are unlikely to occur.

6 Discussion

6.1 Necessity of Multi-parameter Analysis

After the intense rockburst in Case 2, the cumulative MS energy increased gradually and the EI decreased rapidly, accompanied by a gradual increase in the cumulative

apparent volume. Subsequently, a second rockburst occurred. The same changes in the cumulative MS energy, EI , and cumulative apparent volume occurred after the second rockburst. However, no further rockbursts occurred. This result indicates that it is inaccurate to predict rockbursts based only on the evolution characteristics of the above parameters. Therefore, we should comprehensively consider all of the source parameters for the early warning of intermittent rockbursts to improve the accuracy of rockburst prediction. In addition, we should consider other parameters as much as possible on this basis.

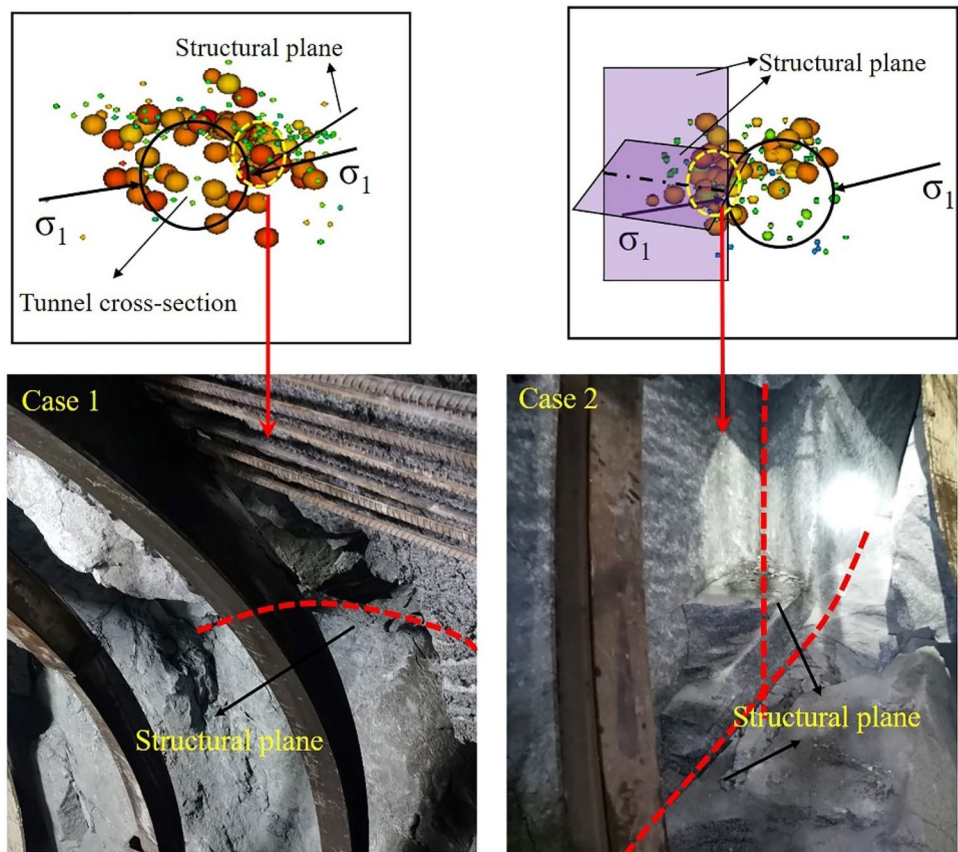
6.2 Influence of Structural Planes on Intermittent Rockbursts

In Sect. 5, it was established that the occurrence of intermittent rockbursts is closely related to the transfer of the stress field. However, the structural plane, as the main controlling factor of rockbursts, may be an important factor for the transfer of the stress field. According to the HSP advance geology exploration results, the integrity of surrounding rock in the tunnel section from mileages K45 + 738 to K45 + 710 m is poor, and the joints are well developed. In the tunnel section from mileages K45 + 630 to K45 + 590 m, the integrity of surrounding rock is poor, and there may be

large-scale structural planes. In Case 1, the orientation of the structural plane was approximately $NS\angle 37^\circ$. In Case 2, the orientations of the two structural planes were approximately $EW\angle 30^\circ$ and $EW\angle 90^\circ$, respectively (See Fig. 15). The existence of structural planes reduced the local rock mass stiffness, allowing the stress to accumulate more readily along the structural planes (Cai and Kaiser 2018). The maximum principal stress intersected the structural planes at a low angle in the cross-section of the tunnel in Case 1 and Case 2, which increased the likelihood of the relative sliding of the rock mass along the structural planes (Hu et al. 2019). The slip of structural planes induced the occurrence of rockbursts. Moreover, the accumulated high stress was difficult to release, resulting in multiple rockbursts along the structural planes.

Based on the distribution characteristics of MS events with different E_s/E_p values described in Sect. 4, the influence of structural planes on intermittent rockbursts can also be briefly discussed. Affected by excavation disturbance, the slip of the structural plane caused some weak protrusions on the structural plane surfaces to be sheared off. Therefore, the type of rock mass failure was dominated by mixed and shear failure in the early stage of the first rockburst. With the stress adjustment, some protrusions with high shear strength became difficult to shear off. The high shear stress acting on

Fig. 15 Distribution of MS events and structural planes around the tunnel in Case 1 and Case 2



the protrusions resulted in the formation of a tensile stress concentration zone in the rock mass near the protrusions. Therefore, the proportion of tensile failure of the surrounding rock mass rapidly increased during this stage. When the protrusions were suddenly sheared off, a large amount of strain energy was released, causing rock ejection and fall of ground in the tunnel. Therefore, the first rockburst occurred in the form of shear failure and was accompanied by shear failure events. After the first rockburst, the stress in the rockburst area was not sufficiently released. As a result, the stress was transferred to the relatively deep protrusions with high shear strength along the structural plane for Case 1, resulting in the formation of a new tensile stress concentration zone in the relatively complete rock mass near the protrusions. With the continuous accumulation of stress, a large number of high-energy tensile failure events occurred. When the protrusions were sheared off, an intense rockburst occurred in the form of shear failure and was accompanied by shear failure events. For the Case 2, stress continued to accumulate in the shallow rock mass. However, the shallow rock mass and protrusions were damaged greatly, and the ability of energy storage was decreased. Therefore, only some relatively low-energy tensile failure events occurred in the shallow rock mass near the protrusions. As the protrusions were sheared off, a moderate rockburst occurred in the form of shear failure and was accompanied by shear failure events. After the second rockburst, the stress in the rockburst area was sufficiently released. During this stage, some shear and mixed failure MS events occurred along the structural plane, and the rock mass tended to become relatively stable.

The above discussion suggests that the occurrence of a large number of tensile failure events after the first rockburst can be used as a characteristic to indicate that another rockburst may occur.

6.3 Selection of Accelerometer Installation Method

The proper layout of the accelerometers is a prerequisite for effectively capturing microcracking signals. The selection of accelerometer installation method in TMB tunneling needs to consider the characteristics of the excavation damage zone (EDZ).

Under high stress, fracturing occurs inside the rock mass, accompanied by the release of stored elastic energy in the form of a stress wave, which can be captured by the MS monitoring system. Therefore, the spatial evolution law of MS events may be a way to reflect the characteristics of the EDZ. Note that the EDZ of the TBM tunnel with a diameter of 12.4 m was analyzed by the acoustic emission monitoring experiment. Based on the different damage degrees, the rock masses in the range of 0–2.7 m and 2.7–9 m away from the tunnel sidewall were divided into macro-fracturing zone and the outer disturbed zone (Li et al. 2011). We analyzed the

characteristics of the EDZ around the tunnel within 15 m before and after two rockburst areas by the spatial distribution characteristics of MS events, as shown in Fig. 15. In the rock mass without structural planes around the tunnel perimeter, most of the MS events were distributed in the range of 0–1 m away from the tunnel sidewall. When there were some structural planes in the rock mass around the tunnel perimeter, the MS events extend along the structural plane to the deep rock mass. MS events in Case 1 and Case 2 were mainly distributed in the range of 0–3.2 m and 0–2.7 m away from the tunnel sidewall, respectively. Based on the above analysis, the macro-fracturing zones of the Case 1 and Case 2 may be determined to be 3.2 m and 2.7 m, respectively. Although this result has not been verified by other exploration methods, it may provide a reference for the selection of accelerometer installation method.

When the integrity of rock mass was good and the joints and fissures were poorly developed, some relatively low-energy MS events occurred in the shallow rock mass, and the risk of rockburst was relatively low during the process of the northern Qinling TBM construction section. In this case, six accelerometers usually were mounted on the tunnel sidewalls using anchoring agents. This new method is simple and it is easy to remove the accelerometers as the tunnel advances. When the structural planes were well developed, the risk of rockburst was relatively high. Moreover, the EDZ around the tunnel may extend along the structural plane to the deep rock mass. To more accurately delineate the rockburst risk area, six accelerometers were installed in the 3.5 m-deep boreholes of the tunnel sidewalls with anchoring agents to reduce the attenuation of wave velocity.

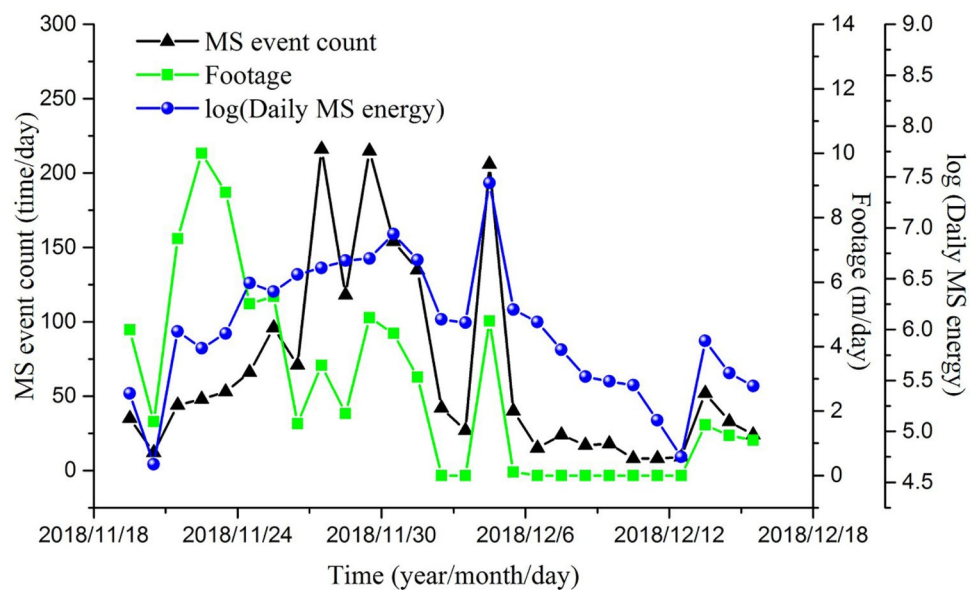
6.4 Preventive Measures for Intermittent Rockbursts Based on MS Monitoring

With intermittent rockbursts, after the first rockburst, workers do not know whether another rockburst will occur in a certain area. With the advancement of the working face, when workers clean the slag in the rockburst area and replace the supporting structures, another rockburst often occurs. This phenomenon seriously threatens the safety of workers. Therefore, based on the results of MS monitoring, a series of measures to prevent intermittent rockbursts are discussed in this section.

First, after a rockburst, we can predict whether another rockburst is likely to occur in the rockburst risk area based on the real-time evolution of the source parameters. In Sect. 4, the precursors of intermittent rockbursts were analyzed in detail.

Second, by reducing the excavation rate, the stress concentration in the rock mass can be effectively reduced, thereby reducing the rockburst risk (Liu et al. 2020; Lu et al. 2018). However, during the excavation process of

Fig. 16 Evolution of microseismicity characteristics with the daily footage variation from November 23, 2018 to December 16, 2018



the northern section of the Qinling tunnel, we found that reducing the excavation rate may not effectively reduce the rockburst risk. Figure 16 shows the microseismicity characteristics with the daily footage variation from November 20, 2018 to December 16, 2018. We can see that the MS event count and daily MS energy increased rapidly with the increase in footage from November 20, 2018 to November 24, 2018. Therefore, an intense rockburst warning was submitted to the construction department. Subsequently, the construction department aimed to reduce the degree of stress concentration by reducing the footage from November 25, 2018 to December 5, 2018. However, the MS event count and daily MS energy further increased during this stage. This result shows that reducing the footage may not effectively reduce the rockburst risk. This conclusion is needed to be further verified. Nevertheless, we still recommend that other prevention measures were needed to be used to reduce the rockburst risk in this case. Subsequently, the construction department stopped excavating the working face and adopt other measures to reduce the rockburst risk.

Third, for a TBM-excavated tunnel, destress drilling can be adopted to fracture localized rock masses (MS event concentration areas), which can effectively release the high stress in a certain area. Some stress release holes were required to pass through the high-stress area (MS event concentration area) from December 6, 2018 to December 13, 2018. Without the influence of excavation disturbance, the MS event count and daily MS energy gradually decreased to a low level during this stage, as shown in Fig. 16. From December 14, 2018 to December 16, 2018, excavation resumed at the working face. The MS event count and daily MS energy decreased significantly compared with those before the excavation was stopped, which indicates that the

stress in the rockburst risk area was effectively released and that only some microcracks occurred. In addition, according to the data recorded by the site engineer, no rockburst occurred in the risk area. The above results indicate that the application of destress drilling is an effective method for reducing the rockburst risk.

Finally, a support system is used to strengthen the surrounding rock mass and protect workers and equipment. Based on the MS monitoring, some valuable guidelines concerning the support forms can be suggested to mitigate the potential rockburst risk. For example, before the second rockburst in Case 2, a large number of MS events were mainly concentrated in 0–2.7 m, and a small number of MS events were concentrated in 2.7–4.4 m. Therefore, the recommended length of the rock bolts should be at least 5.0 m. Based on the MS characteristics, it can be ascertained that an intense rockburst may occur in the near future. Therefore, 22-mm-diameter grouted rebar, H150 steel arches, and 16-mm-diameter pre-fabricated steel mesh slats should be used for rock support. The above support methods have previously achieved good results in the intense rockburst prevention process in the northern section of the Qinling tunnel.

7 Conclusions

In this study, an MS monitoring system suitable for TBM face monitoring was successfully used to monitor the evolution process of rockbursts in real time in the northern section of the Qinling tunnel of the Hanjiang-to-Weihe River Diversion Project. Two typical intermittent rockbursts were studied by analyzing the MS monitoring data. Conclusions can be drawn as follows:

- Similar MS characteristics were observed in Case 1 and Case 2 before the first rockburst: rapid increases in the MS event count and the cumulative MS energy, a rapid increase in the EI accompanied by a sharply increased cumulative apparent volume, and a sharp decrease in the E_s/E_p values. These precursors can be used to provide an early warning of the first rockburst of an intermittent rockburst.
- After the first rockburst in Case 1, the MS event count remained high accompanied by a rapid increase in the cumulative MS energy, while the high-level EI continued to increase accompanied by a rapid increase in the cumulative apparent volume. Moreover, the E_s/E_p values remained low after a short period of fluctuation. The evolution characteristics of these source parameters after a rockburst indicate that a rockburst of the same or higher intensity level as the previous rockburst may occur in the near future. After the first rockburst in Case 2, the MS event count remained high accompanied by a gradual increase in the cumulative MS energy, while the EI decreased rapidly accompanied by a gradual increase in the cumulative apparent volume. In addition, the E_s/E_p values remained low after a short period of fluctuation. The evolution characteristics of these source parameters after a rockburst indicate that a rockburst with a lower intensity may occur in the near future. Thus, these precursors can be used to evaluate whether another rockburst will occur in a certain area after the initial rockburst.
- There were similar MS characteristics in Case 1 and Case 2 after the second rockburst, e.g., a rapid decrease in the MS event count accompanied by a gradual increase in the cumulative MS energy, a sharp drop in the EI accompanied by a gradual increase in the cumulative apparent volume, and a steep upward trend in the E_s/E_p values. These precursors after a rockburst indicate that no rockbursts will occur in that area in the following period.
- After the initial rockburst, some high-energy MS events occurred in relatively deep rock masses of the rockburst area, and the energy stored in the rock mass was not released sufficiently. The relatively deep rock mass of the rockburst area had the capacity to accumulate high stress. Therefore, there is likely to be a further rockburst of the same or higher intensity due to excavation disturbance. However, many low-energy MS events were still recorded in the shallow rock mass, and the energy stored in the rock mass was released to a large extent. The stress-storage capacity of the shallow rock mass was relatively limited. Therefore, there may be another lower-level rockburst due to excavation disturbance.

Acknowledgements The research described in this paper was financially supported by the Chinese National Natural Science Foundation

(No. 51627804, 41941018) and National Key Research and Development Program of China (No. 2018YFC1505301), which is greatly appreciated.

Declarations

Conflict of interest We declare that we do not have any commercial or associative interest that represents a conflict of interest in connection with the work submitted.

References

- Boatwright J, Fletcher JB (1984) The partition of radiated energy between p-wave and s-wave. *B Seismol Soc Am* 74(2):361–376
- Cai M, Kaiser PK, Martin CD (2001) Quantification of rock mass damage in underground excavations from microseismic event monitoring. *Int J Rock Mech Min Sci* 38(8):1135–1145
- Cai M, Kaiser PK (2018) Rockburst support reference book, volume I: rockburst phenomena and support characteristics. MIRARCO, Laurentian University, Sudbury, Ontario
- Chen BR, Feng XT, Ming HJ, Zhou H (2012) Evolution law and mechanism of rockbursts in deep tunnel: time delayed rockburst. *Chin J Rock Mech Eng* 31(3):561–569 ((in Chinese))
- Feng XT, Chen BR, Li SJ, Zhang CQ, Xiao YX, Feng GL, Zhou H, Qiu SL, Zhao ZN, Yu Y, Chen DF, Ming HJ (2012a) Studies on the evolution process of rockbursts in deep tunnels. *J Rock Mech Geotech Eng* 4:289–295. <https://doi.org/10.3724/sp.J.1235.2012.00289>
- Feng XT, Chen BR, Ming HJ, Wu SY, Xiao YX, Feng GL, Zhou H, Qiu SL (2012b) Evolution law and mechanism of rockbursts in deep tunnels: immediate rockburst. *Chin J Rock Mech Eng* 31(3):433–444 ((in Chinese))
- Feng GL, Feng XT, Chen BR, Xiao YX, Zhao ZN (2019a) Effects of structural planes on the microseismicity associated with rockburst development processes in deep tunnels of the Jinping-II Hydro-power Station, China. *Tunn Undergr Sp Tech* 84:273–280. <https://doi.org/10.1016/j.tust.2018.11.008>
- Feng GL, Feng XT, Xiao YX, Yao ZB, Hu L, Niu WJ, Li T (2019b) Characteristic microseismicity during the development process of intermittent rockburst in a deep railway tunnel. *Int J Rock Mech Min Sci*. <https://doi.org/10.1016/j.ijrmm.2019.104135>
- Gibowicz SJ, Young RP, Talebi S, Rawlence DJ (1991) Source parameters of seismic events at the underground research laboratory in Manitoba, Canada: scaling relations for events with moment magnitude smaller Than-2. *B Seismol Soc Am* 81:1157–1182
- Gill DE, Aubertin M, Simon R (1993) A practical engineering approach to the evaluation of rockburst potential Rockburst and Seismicity in Mines. Balkema, Rotterdam, pp 63–68
- Hoek E, Kaiser PK, Bawden WF (2000) Support of underground excavations in hard rock. CRC Press
- Hu L, Feng XT, Xiao YX, Wang R, Feng GL, Yao ZB, Niu WJ, Zhang W (2019) Effects of structural planes on rockburst position with respect to tunnel cross-sections: a case study involving a railway tunnel in China. *B Eng Geol Environ* 79:1061–1081. <https://doi.org/10.1007/s10064-019-01593-0>
- Li SJ, Feng XT, Li ZH, Chen BR, Jiang Q, Wu SY, Hu B, Xu JS (2011) In situ experiments on width and evolution characteristics of excavation damaged zone in deeply buried tunnels. *Sci China Technol Sci* 54(1):167–174. <https://doi.org/10.1007/s11431-011-4637-0>
- Li PX, Feng XT, Feng GL, Xiao YX, Chen BR (2019) Rockburst and microseismic characteristics around lithological interfaces under different excavation directions in deep tunnels. *Eng Geol*. <https://doi.org/10.1016/j.enggeo.2019.105209>

- Liu F, Ma TH, Tang CA, Chen F (2018a) Prediction of rockburst in tunnels at the Jinping II hydropower station using microseismic monitoring technique. *Tunn Undergr Space Tech* 81:480–493. <https://doi.org/10.1016/j.tust.2018.08.010>
- Liu F, Tang CA, Ma TH, Tang LX (2018b) Characterizing rockbursts along a structural plane in a tunnel of the hanjiang-to-weihe river diversion project by microseismic monitoring. *Rock Mech Rock Eng* 52:1835–1856. <https://doi.org/10.1007/s00603-018-1649-0>
- Liu QS, Wu J, Zhang XP, Tang LX, Bi C, Li WW, Xu JL (2020) Microseismic monitoring to characterize structure-type rockbursts: a case study of a TBM-excavated tunnel. *Rock Mech Rock Eng* 53(7):2995–3013. <https://doi.org/10.1007/s00603-020-02111-5>
- Lu CP, Liu Y, Zhang N, Zhao TB, Wang HY (2018) In-situ and experimental investigations of rockburst precursor and prevention induced by fault slip. *Int J Rock Mech Min Sci* 108:86–95. <https://doi.org/10.1016/j.ijrmmms.2018.06.002>
- Ma TH, Tang CA, Tang LX, Zhang WD, Wang L (2015) Rockburst characteristics and microseismic monitoring of deep-buried tunnels for Jinping II Hydropower Station. *Tunn Undergr Space Tech* 49:345–368. <https://doi.org/10.1016/j.tust.2015.04.016>
- Ma TH, Tang CA, Tang SB, Kuang L, Yu Q, Kong DQ, Zhu X (2018) Rockburst mechanism and prediction based on microseismic monitoring. *Int J Rock Mech Min Sci* 110:177–188. <https://doi.org/10.1016/j.ijrmmms.2018.07.016>
- Ma CC, Li TB, Zhang H (2020) Microseismic and precursor analysis of high-stress hazards in tunnels: a case comparison of rockburst and fall of ground. *Eng Geol*. <https://doi.org/10.1016/j.enggeo.2019.105435>
- Mendecki AJ (1993) Keynote address: real time quantitative seismology in mines. In: Proceedings of third international symposium on rockbursts and seismicity in mines 16–18 August 1993. Kingston, Ontario, Canada, pp 287–295.
- Ortlepp WD, Stacey TR (1994) Rockburst mechanisms in tunnels and shafts. *Tunn Undergr Space Tech* 9(1):59–65
- Salvoni M, Dight PM (2016) Rock damage assessment in a large unstable slope from microseismic monitoring-MMG Century mine (Queensland, Australia) case study. *Eng Geol* 210:45–56. <https://doi.org/10.1016/j.enggeo.2016.06.002>
- Tang CA, Wang JM, Zhang JJ (2010) Preliminary engineering application of microseismic monitoring technique to rockburst prediction in tunneling of Jinping II project. *J Rock Mech Geotech Eng* 2(3):193–208. <https://doi.org/10.3724/sp.J.1235.2010.00193>
- Van Aswegen G, Butler AG (1993) Applications of quantitative seismology in South Africa gold mines. In: Proceedings of third international symposium on rockbursts and seismicity in mines, 16–18 August 1993. Kingston, Ontario, Canada, pp 261–266
- Wyss M, Brune JN (1968) Seismic moment stress and source dimensions for earthquakes in California-Nevada Region. *J Geophys Res* 73(14):4681–4694. <https://doi.org/10.1029/JB073i014p04681>
- Xiao YX, Feng XT, Li SJ, Feng GL, Yu Y (2016) Rock mass failure mechanisms during the evolution process of rockbursts in tunnels. *Int J Rock Mech Min Sci* 83:174–181. <https://doi.org/10.1016/j.ijrmmms.2016.01.008>
- Xu NW, Li TB, Dai F, Li B, Zhu YG, Yang DS (2015) Microseismic monitoring and stability evaluation for the large scale underground caverns at the Houziyan hydropower station in Southwest China. *Eng Geol* 188:48–67. <https://doi.org/10.1016/j.enggeo.2015.01.020>
- Xue RX, Liang ZZ, Xu NW, Dong LL (2020) Rockburst prediction and stability analysis of the access tunnel in the main powerhouse of a hydropower station based on microseismic monitoring. *Int J Rock Mech Min Sci*. <https://doi.org/10.1016/j.ijrmmms.2019.104174>
- Zhang CQ, Feng XT, Zhou H, Qiu SL, Wu WP (2012) Case histories of four extremely intense rockbursts in deep tunnels. *Rock Mech and Rock Eng* 45:275–288. <https://doi.org/10.1007/s00603-011-0218-6>
- Zhang SC, Ma TH, Tang CA, Jia P, Wang YC (2020) Microseismic monitoring and experimental study on mechanism of delayed rockburst in deep-buried tunnels. *Rock Mech and Rock Eng* 53:2771–2788. <https://doi.org/10.1007/s00603-020-02069-4>
- Zhou H, Meng FZ, Zhang CQ, Hu DW, Yang FJ, Lu JJ (2015) Analysis of rockburst mechanisms induced by structural planes in deep tunnels. *B Eng Geol Environ* 74(4):1435–1451. <https://doi.org/10.1007/s10064-014-0696-3>

Publisher's Note Springer Nature remains neutral with regard to jurisdictional claims in published maps and institutional affiliations.